optica

Mid-infrared nonlinear optics in thin-film lithium niobate on sapphire

Jatadhari Mishra,[1,†,*] Timothy P. McKenna,[1,†] Edwin Ng,[1,†] Hubert S. Stokowski,[1,†]
Marc Jankowski,[1,2] Carsten Langrock,[1] David Heydari,[1] Hideo Mabuchi,[1]
M. M. Fejer,[1] and Amir H. Safavi-Naeini[1]

[1]*E. L. Ginzton Laboratory, Stanford University, Stanford, California 94305, USA*
[2]*NTT Research Inc. Physics and Informatics Labs, 940 Stewart Drive, Sunnyvale, California 94085, USA*
Corresponding author: jmishra@stanford.edu

Periodically poled thin-film lithium niobate (TFLN) waveguides have emerged as a leading platform for highly efficient frequency conversion in the near-infrared. However, the commonly used silica bottom-cladding results in high absorption loss at wavelengths beyond 2.5 μm. In this work, we demonstrate efficient frequency conversion in a TFLN-on-sapphire platform, which features high transparency up to 4.5 μm. In particular, we report generating mid-infrared light up to 3.66 μm via difference-frequency generation of a fixed 1 μm source and a tunable telecom source, with normalized efficiencies up to 200%/W cm². These results show TFLN-on-sapphire to be a promising platform for integrated nonlinear nanophotonics in the mid-infrared. © 2021 Optical Society of America under the terms of the [OSA Open Access Publishing Agreement](#)

https://doi.org/10.1364/OPTICA.427428

In the past decade, novel mid-IR coherent light sources have developed rapidly, driven by interest in spectroscopic applications [1]. Semiconductor optoelectronic emitters, such as quantum- and interband-cascade lasers have become commercially available, while next-generation mid-IR quantum well emitters and quantum dot emitters seem promising [2,3]. Another class of mid-IR sources is based on frequency conversion in nonlinear optical media. A persistent effort in this area to produce devices with lower physical footprints and higher conversion efficiencies has enabled the steady progress of mid-IR sources from free-space systems [4] to diffused and diced large-core waveguides [5–7] to nanophotonic waveguides and microresonators in thin films [8].

These latter nanophotonic implementations utilize Kerr nonlinearity, which is relatively weak compared to the second-order nonlinearity accessible in competing thin-film platforms; efficient $\chi^{(2)}$-based frequency conversion in the near-IR has been demonstrated in a number of low-loss thin-film waveguide platforms such as lithium niobate (LN) [9], aluminium gallium arsenide [10], and silicon nitride [11]. Thin-film lithium niobate (TFLN) is a mature platform for integrated photonics, that can be readily used to realize both quasi-phase-matched [9] and dispersion-engineered nonlinear interactions [12], as well as high performance electro-optic (EO) devices [13]. As an example, broadband EO frequency-comb generation in the near-IR has been demonstrated in dispersion-engineered LN microring resonators, with octave-spanning EO combs appearing to be feasible [14,15]. Such sources can be extended into the mid-IR, taking advantage of LN's transparency window up to 4.5 μm [16,17]. However, the commonly used silica bottom-cladding layer suffers from significant absorption loss at wavelengths beyond 2.5 μm [18].

In this work, we demonstrate, for the first time, efficient frequency conversion in periodically poled TFLN waveguides bonded to sapphire [19], which feature high transparency up to 4.5 μm [16,20]. We show CW mid-IR second-harmonic generation (SHG) of fundamental wavelengths spanning 2.75–3.27 μm, and estimate normalized SHG conversion efficiencies up to 100%/W cm². Additionally, we demonstrate difference-frequency generation (DFG) between a 1 μm pump and a tunable telecom source to produce CW mid-IR light at wavelengths spanning a range of 2.81–3.66 μm. Normalized conversion efficiencies up to 200%/W cm² are reported for this DFG process in the 2.98–3.32 μm range, over an order of magnitude higher than in periodically poled large-core LN ridge waveguides [21] and approximately 2 orders of magnitude higher than in conventional periodically poled diffused LN waveguides [5].

We first consider the design of the periodically poled TFLN waveguides in Figs. 1(a)–1(c). The simulated normalized efficiencies for DFG of a fixed 1.064 μm pump and a tunable telecom-band signal, for three TFLN waveguide geometries and a 8 μm by 8 μm large-core LN waveguide (similar to that in [21]), all on sapphire substrates, are shown in Fig. 1(b). The simulated efficiencies decrease monotonically with increasing mid-IR wavelength (λ_i) due to their λ_i^{-2} dependence and the increasing area of the mid-IR mode (Supplement 1). DFG efficiency for the 630 nm TFLN drops off faster with λ_i due to a larger portion of the mode being in the cladding, while beyond 1 μm film thickness, the overall DFG efficiency decreases due to larger mode area in the LN. But we see that these TFLN devices can facilitate up to an order of magnitude more efficient DFG than a large-core LN waveguide that may be fabricated via dicing [21]. In this work, we used 630 nm TFLN; thicker films (∼1 μm) may be used for future work involving longer wavelengths in the mid-IR. A comparison of the absorption loss in the mid-IR due to bottom cladding, for
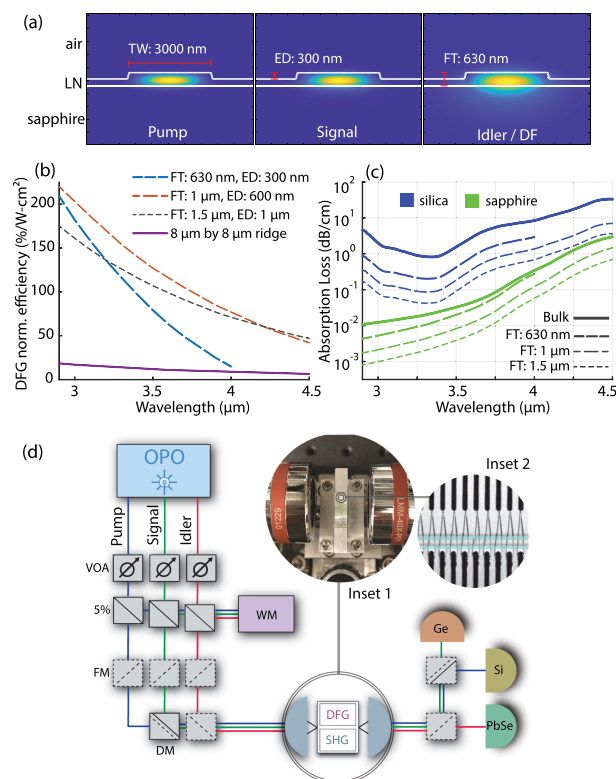
Fig. 1. (a) Simulated fundamental TE mode intensity plots at wavelengths 1.064, 1.62, and 3.1 µm, representing pump, signal, and idler, respectively; TFLN waveguide film thickness (FT), etch depth (ED), and top width (TW) are noted. (b) Simulated DFG (between a fixed 1.064 µm pump, and a tunable telecom-band signal) normalized efficiencies for three TFLN geometries with specified FTs and EDs, and same TWs (3 µm), and for a 8 µm by 8 µm large-core LN waveguide, all on sapphire substrates. (c) Absorption loss in silica versus sapphire bottom-cladding for the same thin-film geometries, simulated from bulk absorption data by calculating the mode overlap with the cladding. (d) Schematic of the experimental setup. Inset 1: chip in the end-firing configuration. Inset 2: two-photon microscope image of periodic poling of TFLN between surface electrodes, with the overlaid lines representing waveguides. VOA, variable optical attenuator; WM, wavelength meter; FM, flip mirror; DM, dichroic mirror.

the previous three TFLN waveguide geometries on silica versus sapphire, simulated from bulk absorption data [22,23], is shown in Fig. 1(c). While going to thicker films can help reduce the loss for a waveguide on either substrate [22], the DFG efficiency is also reduced. As a sapphire substrate has significantly lower absorption loss than silica in the mid-IR, it allows for tightly confining waveguides with high DFG efficiency.

We fabricated the device chip from a 4 in wafer of MgO-doped x-cut 630 nm TFLN on a c-cut sapphire substrate (manufactured by NGK Inc.). To achieve quasi-phase-matching in the 3 µm band, the TFLN was periodically poled with periods in the range of 6.4–7.3 µm using surface electrodes [9]. Ridge waveguides of length ∼5 mm were then fabricated in the poled TFLN using electron-beam lithography and argon-ion milling [19]. Two different nominal top widths, 3.0 µm and 3.3 µm, were chosen for each poling period. The design etch depth was nominally 300 nm, and was measured to be 295 nm with an uncertainty of approximately 5 nm post fabrication. The sidewall angle of the fabricated waveguides was ∼11.5° from normal. In the final fabrication step, the device facets were prepared for end-fire coupling by laser dicing

(DISCO DFL7341) [12]. The waveguides were single-moded in the mid-IR, and a linear taper down to 750 nm top width was added to one side for exciting the fundamental modes at 1 µm and telecom band inputs.

To characterize the TFLN waveguides, we used the output of a tunable CW optical parametric oscillator (OPO) (Toptica TOPO) as shown in Fig. 1(d). Pumped by a 1.064 µm amplified fiber laser, the OPO generated a tunable single-frequency signal (1.45–2.07 µm) and an idler (2.19–4.00 µm) in the ∼0.5−2 W power range. The third output was the residual pump. All three beam paths had variable attenuators for power control, followed by pickoff mirrors leading to a wavelength meter (Bristol 671). Before the waveguide, the three beams were co-aligned in free space via a series of flip and dichroic mirrors. The waveguide setup used reflective objectives (Thorlabs LMM-40X-P01) both to couple into the waveguide chip and to collect the output [Fig. 1(d), Inset 1]. This enabled all three input beams to be focused simultaneously at the input facet without incurring chromatic aberrations. We collected the mid-IR output onto an amplified lead selenide photoconductive detector (Thorlabs PDA20H), the telecom-band output onto a germanium power meter, and the 1 µm output onto a silicon power meter. The setup could be switched between the SHG (idler input) and DFG (pump and signal inputs) configurations.

End-fire coupling via the metallic input objective resulted in ∼1−2% coupling at all three wavelengths. The collection efficiency of the metallic output objective was measured to be ∼25% ± 1% at 1.064 µm, ∼33% ± 1% in the 1.5 µm band, and ∼27.5% ± 2.5% in the 3 µm band. Only fundamental TE modes [Fig. 1(a)] are expected to participate in the SHG and DFG interactions. During beam alignment, the output modes were imaged with cameras to ensure fundamental mode excitations. We expect waveguide propagation losses in the near-IR below 0.2 dB/cm based on quality factor measurements of test resonator devices in this platform (Supplement 1). In the mid-IR, a strongly wavelength-dependent throughput was observed, which was independent of the choice of waveguide and coupling optimizations. We note that no such loss was observed in the near-IR wavelength range, and therefore believe the origin of this loss is absorption due to OH either adsorbed on the surface or in the bulk of the LN film; further investigations of the mechanism are in progress. An absolute loss characterization is not conducted in the mid-IR, but as discussed later, the nonlinear measurements suggest no significant losses in this wavelength range in addition to these relative losses. During characterization, up to 3 W of pump power was incident on the chip, and no facet damage was observed at these power levels.

We observed phase-matched SHG in these nanophotonic devices with the idler from the OPO used as the fundamental spanning 2.75–3.27 µm. For the two different waveguide top widths (3 and 3.3 µm), we plot the fundamental wavelengths corresponding to the peaks of SHG phase matching for 10 different poling periods in Fig. 2(d) (dots). Figures 2(a)–2(c) show three of the corresponding normalized SHG transfer functions (experimental data: dots, theory: dashed lines). We also observed mid-IR DFG spanning 2.81–3.66 µm by mixing a tunable signal beam in the 1.5–1.72-µm wavelength range against the fixed 1.064 µm pump. For the two top widths, we plot the input signal wavelengths that show peak phase matching for mid-IR generation for eight different poling periods in Fig. 2(e) (dots). Normalized DFG transfer functions for a fixed 1.064 µm pump are shown in Figs. 2(f)–2(h) for three devices.
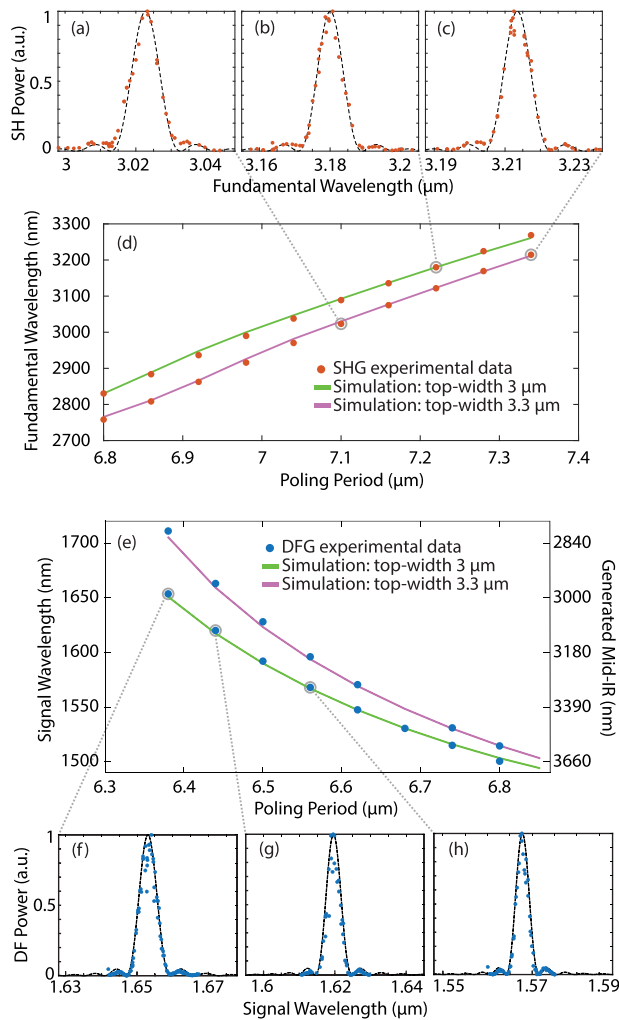
Fig. 2. (a)–(c) Measured SHG transfer functions (dots) versus simulation (dashed lines). (d) SHG phase-matched fundamental wavelength as a function of poling period for two waveguide top widths. (e) DFG phase-matching peak wavelength as a function of poling period for the two top widths; input signal on left axis, generated mid-IR on right axis, for a fixed 1.064 μm pump. (f)–(h) Measured (dots) and simulated (dashed) DFG transfer functions for the fixed pump. Simulations are slightly corrected by an equivalent of ∼20 nm poling period shift.

Based on an analysis of the measured phase-matched wavelengths compared to theoretical predictions, we took an offset of the phase mismatch amounting to an effective poling period shift of ∼20 nm as a fitting parameter to account for small differences between the fabricated and simulated waveguide geometries. After taking this change into account, the shapes of the transfer functions and phase-matching bandwidths closely match simulations for both processes, suggesting a sufficiently high fabrication fidelity over the entire ∼4.1 mm long poled waveguide length. Transfer function simulations taking the wavelength-dependent loss for the mid-IR mode into account did not vary significantly from the lossless case.

We then characterized the normalized efficiency for SHG in each device by tuning the idler output from the OPO to the peak of the SHG transfer function. We varied the first-harmonic (FH) power using a variable attenuator and observed the expected quadratic scaling of the detected second-harmonic (SH) power with input FH. The fundamental and SH powers were measured at the

power meters, and their coupling efficiencies were used to determine their powers in the waveguide, denoted $P_{\mathrm{FH,out}}$ and $P_{\mathrm{SH,out}}$, respectively. Assuming a lossless interaction, the normalized SHG efficiency was estimated as $\eta_{0,\mathrm{SHG}} = P_{\mathrm{SH,out}}/(P_{\mathrm{FH,out}}^2 L^2)$, where L is the interaction length. A similar procedure was adopted for the measurement of the DFG normalized efficiencies. However, instead of changing the input power, which led to thermal drifts, the polarization of the input signal beam was rotated using a half-wave plate to reduce the amount of light coupled into the fundamental TE mode. A polarizer was used to measure the TE component of the transmitted signal. The power and polarization of the input pump beam were held constant. In this measurement, the generated difference frequency (DF) power was observed to be linearly dependent on the signal power in the TE polarization. The normalized DFG efficiency was estimated as $\eta_{0,\mathrm{DFG}} = P_{\mathrm{DF,out}}/(P_{P,\mathrm{out}}P_{S,\mathrm{out}}L^2)$, where $P_{P,\mathrm{out}}$, $P_{S,\mathrm{out}}$, and $P_{\mathrm{DF,out}}$ are the output powers at pump, signal, and DF waves, respectively, and we assumed a lossless process. We estimate that the maximum number of generated mid-IR photons did not exceed 5% of the number of photons in either the signal or the pump beam; this is commensurate with the low-conversion limit assumed in Supplement 1. The maximum generated SH and DF powers in the waveguides were estimated to be in the tens of microwatts.

These estimated SHG and DFG normalized efficiencies, however, needed to be corrected for the wavelength-dependent loss in the mid-IR. We calculated the loss coefficient (α) by assuming that the measured power loss ($e^{-2\alpha L}$) is distributed uniformly over the length of the waveguide L [Fig. 3(a)], and we used this coefficient to estimate the loss-corrected normalized efficiencies. In Supplement 1, we show that in the presence of loss at the long wave, the $\eta_{0,\mathrm{DFG}}$ and $\eta_{0,\mathrm{SHG}}$, previously estimated assuming lossless interactions, may be divided by the factors $(1 - e^{-\alpha L})^2/(\alpha^2 L^2)$ and $(1 - e^{-2\alpha L})^2/(4\alpha^2 L^2 e^{-4\alpha L})$, respectively, to obtain the loss-corrected normalized efficiencies. Without these corrections, the presence of the loss causes a linear reduction of the measured DFG efficiency and a quadratic overestimate of the measured SHG efficiency. Since reductions of the nonlinear coupling due to duty-cycle errors or finite poling depth are shared by both SHG and DFG, the absolute propagation loss may be estimated by taking it as a fitting parameter and setting the mean ratio of the measured to simulated SHG normalized efficiencies equal to its DFG counterpart.

We show the experimentally measured normalized SHG efficiencies (dots) from seven different waveguides, alongside their simulated values (solid line) as a function of fundamental wavelength in Fig. 3(b). Similarly, we plot the experimentally measured normalized DFG efficiencies from three different waveguides (dots), both with and without loss correction, alongside the simulated efficiency values (solid line), as a function of the DFG wavelength in Fig. 3(c). Both the loss corrected SHG and DFG efficiencies are in good agreement with the simulated efficiencies without adding any additional loss to the values estimated using the relative throughput of the waveguide in the mid-IR. This suggests that the estimated α [Fig. 3(a)] is reasonably accurate over the full range of wavelengths measured here. We note, however, that the simulated efficiencies may have up to ±20% uncertainty (Supplement 1), while the measured normalized efficiencies also can only be considered accurate within a few tens of percent, given the uncertainties in the calibration of internal waveguide power
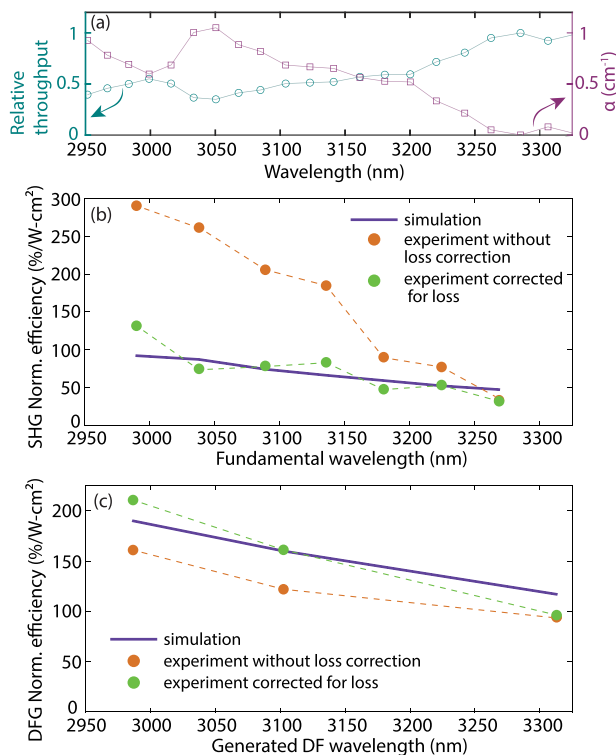
Fig. 3. (a) Normalized waveguide throughput in the mid-IR on left and exponential loss coefficient α on right. (b) and (c) Experimentally measured normalized SHG and DFG efficiencies with and without corrections for the wavelength-dependent loss in the mid-IR, plotted alongside the simulated values.

versus detected output power. An absolute loss measurement in the mid-IR via on-chip resonators and means to reduce it such as thermal processing to drive OH from the waveguide will be the subject of future work [24].

In conclusion, we have demonstrated that periodically poled TFLN on sapphire is a promising platform for both SHG and DFG of mid-IR light due to tight optical confinement, wide transparency range, and large second-order nonlinearity. The resulting normalized efficiencies exceed large-core ridge and diffused LN waveguides by 1 and 2 orders of magnitude, respectively. Future work may involve design of efficient broadband input and output couplers as well as integration of dispersion engineered photonic components and electro-optic components in this platform. The highly efficient three-wave mixing seen here would also allow for effective frequency upconversion of mid-IR light to the 1 um band for detection with silicon detectors, or downconversion of telecom signals to mid-IR for robust free-space optical data transmission, particularly in the atmospheric transmission window around 3.8 μm [5].

Disclosures. The authors declare no conflicts of interest.

Data availability. Raw data underlying the results presented in this paper may be obtained from the authors upon request.

Supplemental document. See Supplement 1 for supporting content.

†These authors contributed equally to this Letter.

REFERENCES

1. N. Picqué and T. W. Hänsch, Opt. Photon. News **30**(6), 26 (2019).
2. Y. Yao, A. J. Hoffman, and C. F. Gmachl, Nat. Photonics **6**, 432 (2012).
3. D. Jung, S. Bank, M. L. Lee, and D. Wasserman, J. Opt. **19**, 123001 (2017).
4. K. C. Burr, C. L. Tang, M. A. Arbore, and M. M. Fejer, Opt. Lett. **22**, 1458 (1997).
5. K.-D. F. Büchter, H. Herrmann, C. Langrock, M. M. Fejer, and W. Sohler, Opt. Lett. **34**, 470 (2009).
6. A. Mayer, C. Phillips, C. Langrock, A. Klenner, A. Johnson, K. Luke, Y. Okawachi, M. Lipson, A. Gaeta, M. Fejer, and U. Keller, Phys. Rev. Appl. **6**, 054009 (2016).
7. A. S. Kowligy, A. Lind, D. D. Hickstein, D. R. Carlson, H. Timmers, N. Nader, F. C. Cruz, G. Ycas, S. B. Papp, and S. A. Diddams, Opt. Lett. **43**, 1678 (2018).
8. A. L. Gaeta, M. Lipson, and T. J. Kippenberg, Nat. Photonics **13**, 158 (2019).
9. C. Wang, C. Langrock, A. Marandi, M. Jankowski, M. Zhang, B. Desiatov, M. M. Fejer, and M. Lončar, Optica **5**, 1438 (2018).
10. L. Chang, A. Boes, P. Pintus, J. D. Peters, M. Kennedy, X.-W. Guo, N. Volet, S.-P. Yu, S. B. Papp, and J. E. Bowers, APL Photon. **4**, 036103 (2019).
11. X. Lu, G. Moille, A. Rao, D. A. Westly, and K. Srinivasan, Nat. Photonics **15**, 131 (2020).
12. M. Jankowski, C. Langrock, B. Desiatov, A. Marandi, C. Wang, M. Zhang, C. R. Phillips, M. Lončar, and M. M. Fejer, Optica **7**, 40 (2020).
13. C. Wang, M. Zhang, X. Chen, M. Bertrand, A. Shams-Ansari, S. Chandrasekhar, P. Winzer, and M. Lončar, Nature **562**, 101 (2018).
14. M. Zhang, B. Buscaino, C. Wang, A. Shams-Ansari, C. Reimer, R. Zhu, J. M. Kahn, and M. Lončar, Nature **568**, 373 (2019).
15. M. Yu, C. Wang, M. Zhang, and M. Loncar, IEEE Photon. Technol. Lett. **31**, 1894 (2019).
16. L. Myers and W. Bosenberg, IEEE J. Quantum Electron. **33**, 1663 (1997).
17. J. He and Y. Li, Opt. Express **28**, 30771 (2020).
18. R. Kitamura, L. Pilon, and M. Jonasz, Appl. Opt. **46**, 8118 (2007).
19. T. P. McKenna, J. D. Witmer, R. N. Patel, W. Jiang, R. V. Laer, P. Arrangoiz-Arriola, E. A. Wollack, J. F. Herrmann, and A. H. Safavi-Naeini, Optica **7**, 1737 (2020).
20. M. E. Thomas, R. I. Joseph, and W. J. Tropf, Appl. Opt. **27**, 239 (1988).
21. L. Lehmann, L. Grossard, L. Delage, F. Reynaud, M. Chauvet, and F. Bassignot, Opt. Express **27**, 19233 (2019).
22. S. A. Miller, M. Yu, X. Ji, A. G. Griffith, J. Cardenas, A. L. Gaeta, and M. Lipson, Optica **4**, 707 (2017).
23. B. S. Patel and Z. H. Zaidi, Meas. Sci. Technol. **10**, 146 (1999).
24. J. R. Schwesyg, C. R. Phillips, K. Ioakeimidi, M. C. C. Kajiyama, M. Falk, D. H. Jundt, K. Buse, and M. M. Fejer, Opt. Lett. **35**, 1070 (2010).